Agricultural and Forest Meteorology 264 (2019) 164–177

Contents lists available at ScienceDirect

Agricultural and Forest Meteorology

journal homepage: www.elsevier.com/locate/agrformet

Continuous observation of vegetation canopy dynamics using an integrated low-cost, near-surface remote sensing system

Jongmin Kim[a], Youngryel Ryu[a,b,c,d,*], Chongya Jiang[d], Yorum Hwang[a]

[a] Interdisciplinary Program in Landscape Architecture, Seoul National University, Republic of Korea
[b] Departments of Landscape Architecture and Rural Systems Engineering, Seoul National University, Seoul, Republic of Korea
[c] Interdisciplinary Program in Agricultural and Forest Meteorology, Seoul National University, Republic of Korea
[d] Brain Korea 21 Plus Team, Seoul National University, Republic of Korea

ARTICLE INFO

Keywords:
Leaf area index
NDVI
EVI
fPAR
LED
Camera

ABSTRACT

Continuous monitoring of vegetation indices (VIs) the fraction of absorbed photosynthetically active radiation (fPAR) and leaf area index (LAI) through satellite remote sensing has advanced our understanding of biosphere–atmosphere interactions. Substantial efforts have been put into monitoring individual variables in the field, but options to concurrently monitor VIs, fPAR, and LAI in-situ have been lacking. In this paper, we present the Smart Surface Sensing System (4S), which automatically collects, transfers and processes VIs, fPAR and LAI data streams. The 4S consists of a microcomputer, controller and camera, a multi-spectral spectrometer built in with a light-emitting diode (LED) and an internet connection. Lab testing and field observations in a rice paddy site that experiences wet summer monsoon seasons confirmed the linear response of 4S to light intensities in the blue, green, red and near-infrared spectral channels, with wide ranging temperatures and humidity having only a minor impact on 4S throughout the growing season. Applied over an entire rice growing season (day of year [DOY] 120 - 248), VIs and fPAR from 4S were linearly related to corresponding VIs from a reference spectrometer (R^2 = 0.98; NDVI, R^2 = 0.96; EVI) and the LAI-2200 instrument (R^2 = 0.76), respectively. Integration of gap fraction-based LAI from LED sensors and a green index from the micro-camera allowed tracking of the seasonality of green LAI. The continuous and diverse nature of 4S observations highlights its potential for evaluating satellite remote sensing products. We believe that 4S will be useful for the expansion of ecological sensing networks across multiple spatial and temporal scales.

1. Introduction

Vegetation indices (VIs), the fraction of absorbed photosynthetically active radiation (fPAR) and leaf area index (LAI) represent key structural and functional variables within a canopy (Sellers et al., 1997). These variables describe light interception by plant canopies (Baldocchi et al., 1984; Myneni et al., 1987; Ross, 1981), vegetation activity (Tucker, 1979) and carbon/water fluxes (Baldocchi et al., 2002; Leuning et al., 1995; Monteith, 1965; Ryu et al., 2011). Satellite remote sensing provides maps of these variables through space and time, which help elucidate the response of vegetation to climate change (Jiang et al., 2017; Myneni et al., 1997).

VIs, fPAR, and LAI have been independently monitored using near-surface sensors. For example, a rotating hemispherical spectrometer has been used to monitor VIs in a rice paddy and a deciduous forest (Motohka et al., 2009; Nagai et al., 2014a). A spectral system integrating a spectrometer, a pan-tilt unit and a camera was developed to measure spectral reflectance at different angles from a tower in a coniferous forest (Hilker et al., 2007). A light-emitting diode (LED) was used to function as a spectrally selective light detector which measures spectral reflectance and monitors VIs in a savanna, evergreen and deciduous forests (Ryu et al., 2014, 2010c). Low-cost spectral reflectance sensors were used to monitor PRI and NDVI of vegetation continuously (Garrity et al., 2010; Magney et al., 2016). In addition, networked digital cameras and ground-based spectrometers have been used to create networks for monitoring canopy color and VIs at ecosystem scales (Gamon et al., 2006; Richardson et al., 2018). To observe fPAR, multiple upward and downward-facing quantum sensors have been posi-

* Corresponding author at: Department of Landscape Architecture and Rural Systems Engineering, Seoul National University, Seoul, 151-921, Republic of Korea.
E-mail address: yryu@snu.ac.kr (Y. Ryu).

https://doi.org/10.1016/j.agrformet.2018.09.014
Received 21 March 2018; Received in revised form 14 September 2018; Accepted 17 September 2018
Available online 22 October 2018
0168-1923/

tioned above and below a forest canopy (Inoue et al., 2008; Jenkins et al., 2007). Various sensors have been developed and installed to monitor LAI, including an upward-facing digital camera (Ryu et al., 2012) and quantum sensor systems that measure light attenuation through canopies (Qu et al., 2014a; Yin et al., 2017) as well as photodiodes installed at an angle of 57 degrees (Fang et al., 2018; Raymaekers et al., 2014). However, the continuous and concurrent in-situ observation of these variables through one instrument has not previously been attempted.

Quantifying green LAI is important in order to effectively estimate photosynthesis, but it remains a challenge (Gitelson et al., 2014). In plants, photosynthesis occurs in green leaves where chlorophyll is found. In particular, quantifying green LAI is essential to estimating crop photosynthesis (Gitelson and Gamon, 2015), as yellow leaves and stems may account for a large part of the total LAI (Fang et al., 2014). Commonly used optical sensors based on gap fraction theory, such as the LAI-2200 cannot distinguish green leaves from those of other colors (Chen et al., 1997). Although the downward looking digital images inclined at 57.5 degree were used to monitor green LAI, this method required the use of a 3D plant architecture model (Baret et al., 2010). Therefore, a destructive method, which requires considerable labor, time and effort, has been commonly used to quantify green LAI (Huang et al., 2018).

Recent advances in microcomputers and controllers have improved our ability to quantify VIs, fPAR and LAI by providing the opportunity to concurrently monitor these measurements in-situ. However, the accessibility of this continuous observation of biophysical variables has been limited by high equipment costs and labor requirements for collecting and processing data. A microcomputer containing a microprocessor is a relatively small and inexpensive device. For example, Liao et al. (2017) developed a system to monitor the growth of orchids with an integrated microcomputer and micro-camera. Ferrández-Pastor et al. (2016) measured humidity and temperature using a microcomputer. Data processing and transfer can become less time consuming and labor intensive when the microcomputer is connected to Internet (Gressler et al., 2015). A microcontroller, which is much cheaper than conventional micrometeorological data loggers, converts the analog signal from the sensors into digital data that can be saved to the computer and it also controls the timing and frequency of the data's acquisition. A recent study quantified the rate of plant growth by using a commercially available microcontroller to accurately measure string length changes (Zhen et al., 2017).

Integrating a microcomputer, camera and controller can help the development of cost-effective canopy monitoring systems. Near-surface sensors, which have relatively small footprints compared to satellite pixel sizes or eddy covariance footprints, must be installed in multiple locations to obtain spatially representative values (Richardson et al., 2013; Ryu et al., 2012). Recently, researchers have attempted to develop cost-effective spectrometers using photodiodes and LEDs (Bauer et al., 2014; Garrity et al., 2010; Qu et al., 2014b; Ryu et al., 2010a; Yin et al., 2017). Although the cost of spectral sensors has decreased, the complete system including data processing, storage, and sharing is still not that cost-effective. For example, inexpensive LED sensors were combined with commercially available and widely used data loggers and laptops that were much more expensive than the LED sensors (Ryu et al., 2010a, 2014). Microcomputers and controllers are an inexpensive alternative for tasks such as data collection, storage, and processing, typically performed by conventional data loggers and computers.

In this study, we developed a Smart Surface Sensing System (4S) that concurrently monitors canopy color, VIs, LAI, and fPAR and then automatically collects, transfers, and processes the data. This system consists of a microcomputer, a microcontroller, a multi-spectral spectrometer built from an LED, a micro-camera and an Internet connection. In this paper, we 1) describe the 4S, 2) report its performance in terms of the linear response to varying light intensities as well as sensitivity to temperature and humidity, 3) evaluate 4S-derived VIs, fPAR, and LAI data collected in a rice paddy with data from a set of reference instruments.

2. Materials and methods

2.1. Development of the 4S

The 4S consists of a Raspberry Pi microcomputer (Raspberry Pi b2 module, Raspberry Pi Foundation, Cambridge, UK), Arduino microcontrollers (Arduino Nano, Arduino, New York, NY, USA), a multi-spectral spectrometer built from LEDs, a micro-camera (Camera module v2, Raspberry Pi) and an Internet connection. The Raspberry Pi microcomputer controls the automated workflow chain, connecting all components.

To measure spectral intensity with 4S, we upgraded the LED circuit used by Ryu et al. (2010a) by changing the power supply, as the microcontroller provided a more stable supply of electricity to the amplifier (op-amp LTC1060). We tested and selected LEDs that could detect light at the desired wavelengths (see section 2.2) and then connected the LED, amplifier, capacitor, and Arduino microcontroller together. When the LED detects light, electrons are excited, which alters the voltage flowing through the amplifier and capacitor and then the Arduino microcontroller translates the analog signal to a digital number (DN). The Raspberry Pi microcomputer collects images from the micro-camera and spectral intensity data from the LED. Data are then transferred to a remote server using file transfer protocol (FTP; Fig. 1). The microcomputer has four USB ports, so we can combine up to four microcontrollers. In addition, the microcontroller can control two LED circuits simultaneously. Therefore, although only one LED circuit is connected in the (Fig. 2), up to 8 LED circuits can be coupled to the microcomputer. The list and price of parts appear in Appendix A. One pair of 4S costs $218.8 (as of Aug. 2018).

2.2. Calibrating and evaluating the LED

To select an LED with spectral wavebands in the red, green, blue and near infrared (NIR) domains matching the MODIS spectral bands (http://modis-sr.ltdri.org/guide/MOD09_UserGuide_v1.4.pdf), we tested a wide range of LEDs using a solar cell chamber (K3100 solar cell IPCE measurement system, Mc Science, Suwon, Korea), which emits spectrally

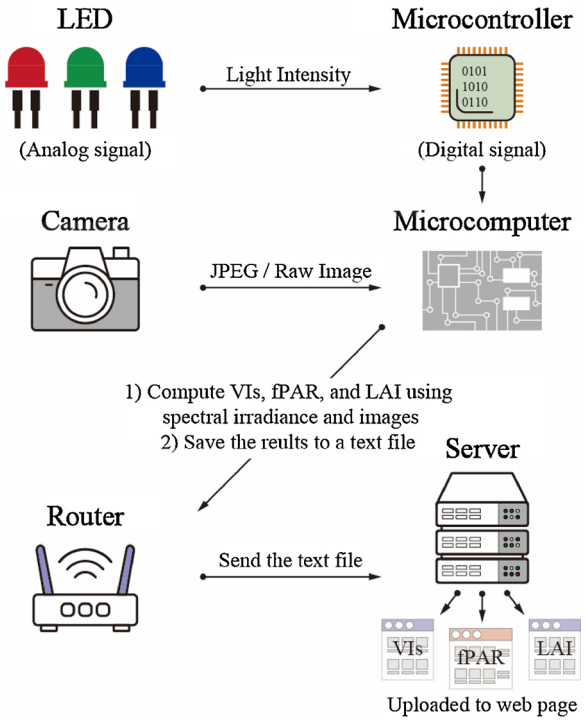

Fig. 1. Automated workflow of the Smart Surface Sensing System (4S).

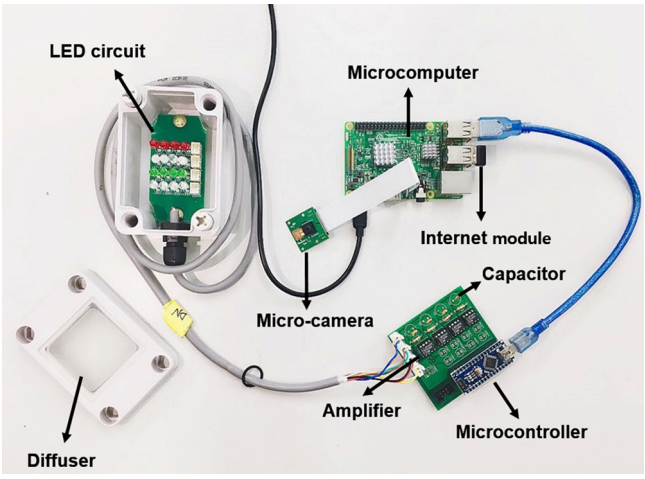

Fig. 2. The Smart Surface Sensing System (4S). All components are connected, and the microcomputer controls the automated data workflow.

Table 1
Light-emitting diode (LED) sensor specifications compared to MODIS.

Spectral band	Peak sensitivity	Full Width at Half-Maximum (FWHM)	MODIS
Blue	412 nm	59 nm	459–479 nm
Green	560 nm	42 nm	545–565 nm
Red	656 nm	44 nm	620–670 nm
Near-infrared	850 nm	100 nm	841–876 nm

selected light. We determined LED voltages that responded to the solar cell chamber with wavelengths of 300–700 nm at 2-nm intervals and 700–900 nm at 50-nm intervals, thereby enabling us to quantify the spectral response of each LED (Table 1). From more than five available wavelengths in commercial LEDs, we selected LEDs based on their spectral responses that were most similar to MODIS wavelength range in the four channels. To ensure that incoming light was fully diffused inside the LED head enclosure, we covered the LED sensors with Teflon to measure spectral irradiance (Fig. 2).

To calibrate the LED sensors, we compared the voltages produced by the LEDs to the spectral irradiance readings from a spectrometer (FieldSpec 4 Wide-Res Field Spectroradiometer, ASD, Inc., Boulder, CO, USA) across a wide range of radiation intensities. On a day with clear skies (DOY 223 in 2016), we installed LEDs and the spectrometer with the fiber optics covered by a cosine corrector, together on an open rooftop at Seoul National University in order to minimize the effects of shadows from surrounding structures. The sensors were placed the zenith. We collected data throughout the day under solar irradiance ranging from 60 to 1000 W m^{-2}. We extracted spectral irradiance values from the spectrometer over spectral wavelength ranges corresponding to the Full Width at Half-Maximum (FWHM) of each LED and averaged the values to calibrate the LED sensors. Digital numbers from 4S LED sensors exhibited strong linear relationships with spectral irradiance values from the spectrometer in the blue, green, red, and NIR bands (Fig. 3). We found that the linear relationships were tightly consistent over the whole growing season in the rice paddy site (Appendix B).

To monitor fPAR, we combined red, green and blue LEDs to determine PAR (Eq. 1). We applied a linear regression model to the red, green, and blue LED readings (DOY 179 to 185 in 2016, every 30 min) to estimate PAR. This period included cloudy and clear sky conditions to compare PAR ranging from 0 to 2000 umol m^{-2} s^{-1}. After calibrating three regression coefficients against a reference PAR quantum sensor (PQS 1; Kipp & Zonen B.V., Delft, The Netherlands) (Eq. 1), we obtained a strong linear relationship (R^2 = 0.99, Bias = 3.8%, RMSE = 11%; Fig. 4). In addition, when we compared the readings of the PAR sensor and 4S across the entire growing season in the rice paddy site, we confirmed that their relationships were highly linear (R^2 > 0.97) with little bias (relative bias < 6%).

$$PAR = \alpha \times red + \beta \times green + \gamma \times blue \quad (1)$$

where α, β, and γ are parameters, and red, green, and blue are LED band readings.

2.3. Testing the 4S in a rice paddy field

2.3.1. Site description

Our site is located in Cheorwon (38.2013 °N; 127.2507 °E), the center of the Korean Penisula, is an intermittently irrigated rice paddy that is also part of the KoFlux (Yang et al., 2018). The annual maximum, minimum, mean air temperature and total precipitation (for 2000–2014) were 35.3 °C, –12.3 °C, 10.2 °C, and 1391 mm, respectively (Korean Meteorological Administration weather station data collected 8 km from the study site). The site is under a shared management regime and covers an area of 3528 m^2 (98 × 36 m). We installed an iron deck that was 0.8 m high and 9.5 m long in the rice paddy (Fig. 5). The species of rice cultivated at this site were *Oryza sativa L* and *cv. Odae 1ho*. The rice canopy was continuously monitored from May to September 2016. Rice seedlings were grown in a greenhouse for twelve days, transplanted to the field on DOY 120, and then harvested on DOY 248. Stem density was 17 ± 1.5 plant m^{-2} (mean ± 95% confidence interval (CI)).

2.3.2. 4S installation, data collection, and data processing

The 4S was installed on three horizontal booms 2 m above the ground. One LED sensor was oriented to the zenith, and the other toward the nadir (Fig. 5b). We cross-calibrated each spectral band reading between the upward and downward LED sensors in the field before transplantation. By attaching Teflon to both the upward- and downward-facing sensors, we measured spectral irradiance in both directions, obtaining a bi-hemispheric spectral reflectance. We calculated the normalized difference the vegetation index (NDVI) and enhanced the vegetation index (EVI) using 4S-derived spectral reflectance data (Huete et al., 2002; Tucker, 1979):

$$NDVI = \frac{\rho NIR - \rho red}{\rho NIR + \rho red} \quad (2)$$

$$EVI = \frac{G \times (\rho NIR - \rho red)}{\rho NIR + C_1 \times \rho red - C_2 \times \rho blue + L} \quad (3)$$

where ρ represents the spectral reflectance, G represents a gain factor, C_1 and C_2 represent the coefficients of the aerosol resistance term, and L represents the soil adjustment factor. We followed the MODIS EVI algorithm, where L = 1, C_1 = 6, C_2 = 7.5, and G = 2.5 (Huete et al., 2002; Jiang et al., 2008). We collected LED data with 9600 bps and we saved the average of one minute data using the microcomputer. NDVI and EVI were computed every minute and averaged over half-hourly. To compare 4S and Jaz spectrometer that had a wide footprint (180 °), we averaged the data from the four pairs of LEDs.

To quantify fPAR, incoming, reflected, and transmitted PAR (Eq. (4)), we used three sets of LED sensors installed on the iron deck. Incoming and reflected PAR were monitored from the same three booms as NDVI and EVI (Fig. 5b). To measure transmitted PAR over the intermittently irrigated rice paddy, an LED sensor was fixed, with each 4S, on a Styrofoam float that moved vertically with the water table

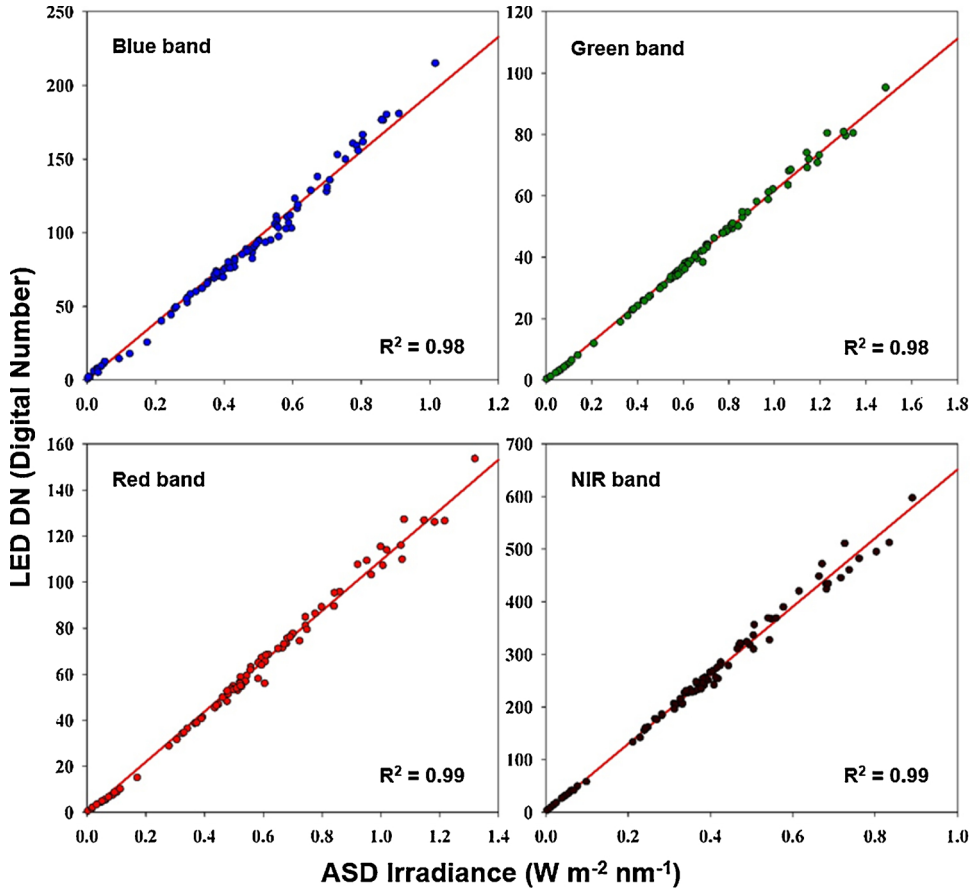

Fig. 3. Calibration of Light-Emitting Diodes (LEDs) against an ASD spectrometer across a wide range of solar radiation conditions (60 – 1000 W m-2) on a day with clear skies. The red lines indicate linear regressions.

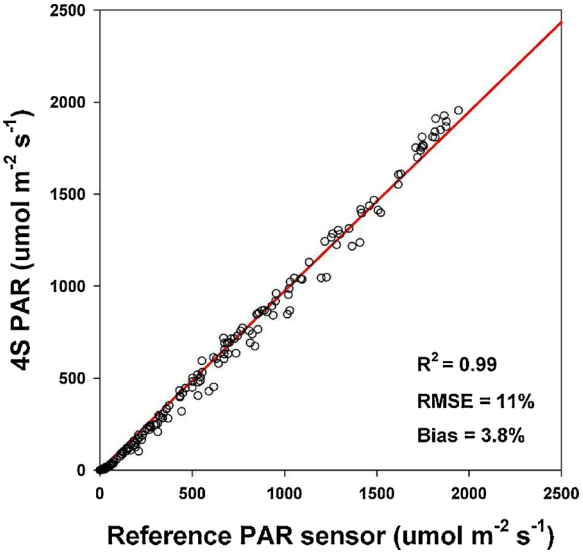

Fig. 4. Linear relationship between the Smart Surface Sensing System (4S) Photosynthetically Active Radiation (PAR) estimates and those of a reference PAR sensor.

inside a square vertical steel frame. If no water was present, it rested on the soil surface. LED sensors were installed under the canopy after DOY 167 because the height of the rice canopy was smaller than the height of the sensor enclosure. Data was used only from 08:00 to 18:00 to avoid low-light conditions. LED data was collected in 1-minute intervals and the half-hourly fPAR was averaged using data from all three sets. The fPAR was calculated as shown below (Eq. (4)). In addition, we installed a quantum sensor to measure total PAR and diffuse PAR (PAR_{dif}) at 7 m height in the flux tower. To measure $PAR_{dif,}$ a rotating wing was installed to create shadows that blocked the direct beam incident on the quantum sensor to separate beam and diffuse components (Michalsky et al., 1986; Michalsky, 1988).

$$fPAR = \frac{(PAR_{inc} - PAR_{out} - PAR_{transm})}{PAR_{inc}} \quad (4)$$

where PAR_{inc} is incoming PAR, PAR_{out} is outgoing PAR, and PAR_{transm} is PAR transmitted through the canopy.

To quantify LAI of the rice paddy, we measured the gap fraction (GF) of incoming spectral irradiance from the blue band of the LED sensors above and below the canopy, as the blue band minimizes the scattering effect of canopy (Brusa and Bunker, 2014; Welles and Norman, 1991). To reduce noise in daily LAI time series, data from diffuse sky conditions without sun flecks were chosen, which leads to a heterogeneous radiation field. Sky conditions were categorized as diffuse when the ratio of PAR_{dif} to PAR was more than 75%.

$$LAI = \frac{-ln(\bar{GF})}{k \times \Omega_e} \quad (5)$$

where k is the extinction coefficient under diffuse sky conditions (see Appendix C) and Ω_e is the element clumping index. To estimate hemispheric Ω_e under diffuse sky conditions, clear sky days were first defined as those with a daily mean ratio of PAR_{dif} to PAR below 50%.

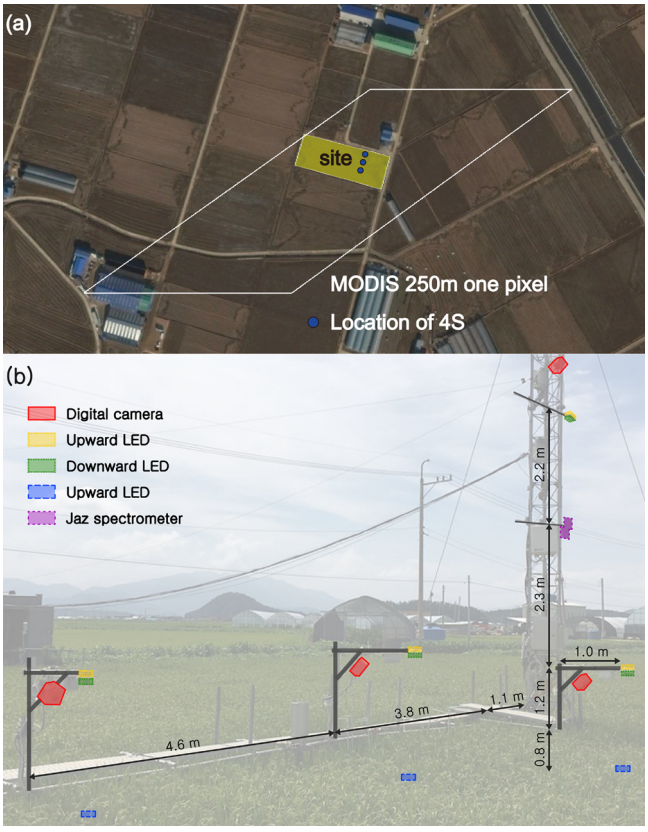

Fig. 5. (a) Site map. The white parallelogram marks the boundary of a MODIS 250-m pixel. The yellow rectangle is the monitored rice paddy site and the blue dots represent the different locations of the Smart Surface Sensing System (4S). (b) Deployment of 4S in the field. A total of four 4S sets, each with a reference spectrometer, were installed on the site.

Next, measurements were taken of paired samples of GF with solar zenith angles at 15° intervals from 0 to 90°in the morning and afternoon. Finally, the Ω_e corresponding to each angle was calculated using the ratio of $\ln[GF(\theta)]$ to $ln[GF(\theta)]$, where θ is the viewing zenith angle (Lang and Yueqin, 1986; Ryu et al., 2010b). Hemispheric Ω_e was estimated by multiplying Ω_e with the weighting factor ($\sin\theta\cos\theta$) for each 15° intervals. The over bar indicates averaged data from the three sets.

To convert LED LAI to green LAI (LAI_g), the Greenness Index (GI) was quantified using three digital cameras on the iron deck (Eq. (6)). The micro-cameras installed on the booms 2 m above the ground (Fig. 5b) viewed the canopy at a 57° angle. To capture images that were not affected by shadows from the structure, the microcomputer was programmed to take images at 06:00, 12:00, and 18:00 each day at their respective location and we covered the mask to see only rice canopy (Appendix D). GI was calculated as in Eq. (6)(Nagai et al., 2014b; Richardson et al., 2007; Sonnentag et al., 2012). After calculating GI for each image, the highest GI was selected for each day from each plot to minimize noise. To estimate LAI_g, the normalized GI was multiplied by LAI (Eq. (7)), starting on DOY 209, when GI began to decrease.

$$GI = \frac{DN_g}{(DN_r + DN_g + DN_b)} \quad (6)$$

where DN_r is red DN, DN_g is green DN, and DN_b is blue DN.

$$LAI_g = LAI \times normalized\ GI \quad (7)$$

2.3.3. Reference data collection

To evaluate 4S-derived LAI and LAI_g, we collected six rice hills around the tower randomly every two weeks (Huang et al., 2018). The rice hill is a bundle unit of rice when it is planted. First, leaves from three rice hills were scanned and weighed in the laboratory. The leaves were attached to a white board and scanned images were created and saved at 300 dpi in JPEG format using a CanonScan LiDE 120 laser scanner. To analyze these images, we differentiated between green and yellow leaves by extracting the blue channel from the JPEG image using MATLAB. We visualized each blue-channel image and applied different thresholds. The remaining three hills were dried at 80 °C for 48 h and we measured their weight to estimate the LAI based on leaf mass per unit area. The ratio of green leaves to total leaves was then calculated from three samples and this ratio was applied to the remaining three samples. Thus, we calculated destructive total LAI (LAI_t) as well as destructive green LAI (LAI_g). During the reproductive and ripening stages, we measured grain weight and hemi-surface grain area (Chen and Black, 1992; Lang, 1987).

To evaluate 4S-derived VIs, a Jaz spectrometer was installed on the tower (Ocean Optics, Dunedin, FL, USA) at a height of 5 m. The Jaz spectrometer, which covers a spectral range of 350 to 1033 nm at 1-nm resolution, was kept in a temperature-controlled enclosure (400 BTU (DC); EIC Solutions, Warminster, PA, USA) at 23 °C with a desiccant to maintain dry conditions, as variations in temperature and humidity could influence the performance of the CCD array in the spectrometer (Price et al., 2014). The spectrometer was connected to two fibers covered with a cosine corrector to measure spectral irradiance. We calibrated the Jaz spectrometer monthly with an HL-2000-CAL light source (Ocean Optics, Dunedin, FL, USA). The spectral reflectance data that was recorded by the Jaz spectrometer was saved at 1-min intervals. For comparison with the daily pattern of NDVI and EVI values from the Jaz spectrometer and 4S, we utilized noontime spectral reflectance values from the Jaz spectrometer to calculate NDVI and EVI.

The LAI-2200 Plant Canopy Analyzer (LI-COR, Lincoln, NE, USA) was used to evaluate 4S fPAR and LAI estimates. We randomly collected LAI-2200 data at more than 25 points every two weeks before noon. At each point, we measured incoming and reflected light above the canopy and transmitted light below the canopy. For measurement below the canopy, we held the LAI-2200 less than 5 cm above the soil or water surface. We used a 90° view cap to reduce noise from the operator. The weight factor was multiplied by five ring widths (7° = 0.041, 23° = 0.131, 38° = 0.201, 53° = 0.290, and 68° = 0.337) to calculate the hemispheric light intensity and then fPAR was quantified using Eq. 4. To quantify LAI with scattering correction, we used FV2200 software (LI-COR, Lincoln, NE, USA) with data collected from the LAI-2200 (Kobayashi et al., 2013).

2.3.4. Satellite remote sensing data

We compared field observations to satellite data with different spatial resolutions, including MODIS Terra, MODIS Aqua, Landsat 8, and Sentinel-2 Level 2 A images. We used MODIS surface reflectance products (MOD09GQ and MYD09GQ), which have a daily interval and 250-m resolution. We only used data that was classified as (a) ideal quality, i.e., “MODLAND QA bits” (00) in the MOD09GQ QA description; (b) cloud free in “cloud state” (00) and “pixel adjacent to cloud” (0); and (c) low or average aerosol quantity, i.e., “aerosol quantity” (01 or 10) in the 1-km QA of MOD09GA products (Ryu et al., 2014; Zhao and Running, 2010). For the Landsat 8 imagery (30-m resolution, 16-

Table 2
Percentage of dates during the growing season that were monitored by 4S.

	System 1	System 2	System 3	On tower	Average
LEDs	63 %	87 %	79 %	74 %	76%
57 °Cameras	73 %	73 %	86 %	88 %	80%

day revisit time), we downloaded surface reflectance products and removed images with cloud cover above 30%, which was visually confirmed for each image. We removed images with cloud cover using a similar processing protocol to the Landsat 8 post-processing, when dealing with Sentinel-2 (10-m resolution, 10-day revisit time) imagery. For atmospheric correction, terrain correction and cirrus correction of Sentinel-2 A Level 1C (L1C) imagery, we applied the Sen2cor (Version 2.3.0) function in Sentinel Application Platform (SNAP) software and generated Level 2 A (L2 A) data.

3. Results and discussion

3.1. General performance

4S achieved a high rate of data acquisition throughout the growing season including the wet monsoon summer period. We collected LED data with 9600 bps and we saved the average of one minute data using the microcomputer. The half-hourly data was calculated using the 1-minute interval data in the lab. To quantify how well 4S collected data, we used the fraction of days for which data was available during the growing season (see Table 2). The LEDs and camera were able to collect data for 76% and 80% of days in the growing season, respectively. Unexpected data gaps occurred due to an interruption of the electricity supply caused by lightning, water leakage into the 4S and a malfunctioning of the SD memory card. To overcome these issues, the status of the 4S was checked every day via the internet, and if any problem was detected, we returned to the site as soon as possible to fix it.

The LED sensors worked well in a broad range of temperature (10–35 °C, Fig. 6 (a)) and relative humidity (20–100%, Fig. 6 (b)). When we compared the incoming DN from the Jaz spectrometer (840–860 nm) in a temperature controlled enclosure and the NIR band of the LED sensor, 4S exhibited a linear relationship with the Jaz spectrometer (R^2 = 0.98). The strong linear relationship between Jaz and LED readings over the entire growing season confirmed that our inexpensive 4S LED sensors (Appendix A) are robust and reliable instruments for monitoring canopy structure and function under a wide range of environmental conditions.

3.2. Seasonal variations in VIs, fPAR and LAI

The 4S LED sensors and Jaz spectrometer produced well matched VI values during the growing season (R^2 > 0.96, relative bias < 3%; Fig. 7). NDVI and EVI values increased after DOY 140. During DOY 160–209, NDVI was nearly saturated, whereas EVI continued to increase, consistent with results from a previous study (Mutanga and Skidmore, 2004). From the beginning of the ripening stage (DOY 209) and onward, both NDVI and EVI decreased (Fig. 7). The NDVI and EVI values dropped suddenly after harvest (DOY 248). VI values from 4S and Jaz spectrometer differed slightly around the transplanting date (Fig. 7b and d). We assume that spatially heterogeneous water turbidity (Motohka et al., 2009) might lead different VI values between the two sensors because of their different footprints.

4S-derived fPAR exhibited magnitude and seasonal patterns consistent with LAI-2200-derived fPAR (R^2 = 0.76, Bias = 0.014, RMSE = 0.06, Fig. 8). Three 4S-derived fPAR datasets were compared to > 25 points of corresponding estimates from the LAI-2200. Before DOY 167, we could not calculate fPAR because the depth of sensor enclosure was larger than the height of the rice canopy above water surface. Just after the 4S fPAR system was installed (DOY 167), discrepancies in fPAR between the 4S and LAI-2200 were apparent. We assume that the methodological difference in data collection between LAI-2200 and 4S could form a bias. We collected more than 25 points of fPAR data over the rice paddy using the LAI-2200, whereas the 4S was fixed at three plots to monitor fPAR. After DOY 180, LAI-2200 and 4S showed consistent fPAR values.

4S LAI and LAI_g were similar in magnitude and seasonal pattern to the LAI reference values, such as LAI_t, LAI_g by destructive method and LAI measured by LAI-2200 during the growing season (Fig. 9). Among reference LAI, the LAI derived by LAI-2200 had the highest R^2 value with 4S LAI over the whole growing season (R^2 = 0.71). The timing and magnitude of the maximum LAI value shows that LAI_t was 5.9 on DOY 190, LAI_g was 5.7 on DOY 190, LAI-2200 LAI was 5.9 on DOY 201, and 4S LAI and LAI_g were 5.11 on DOY 201. During the ripening stage, 4S LAI showed a similar magnitude to LAI-2200 LAI (bias = –2%), whereas 4S LAI was overestimated compared to LAI_t (bias = 25%) and destructive LAI_g (bias = 69%). When we compared 4S LAI_g to reference LAI during the ripening stage, the relative bias was lowest with LAI_g

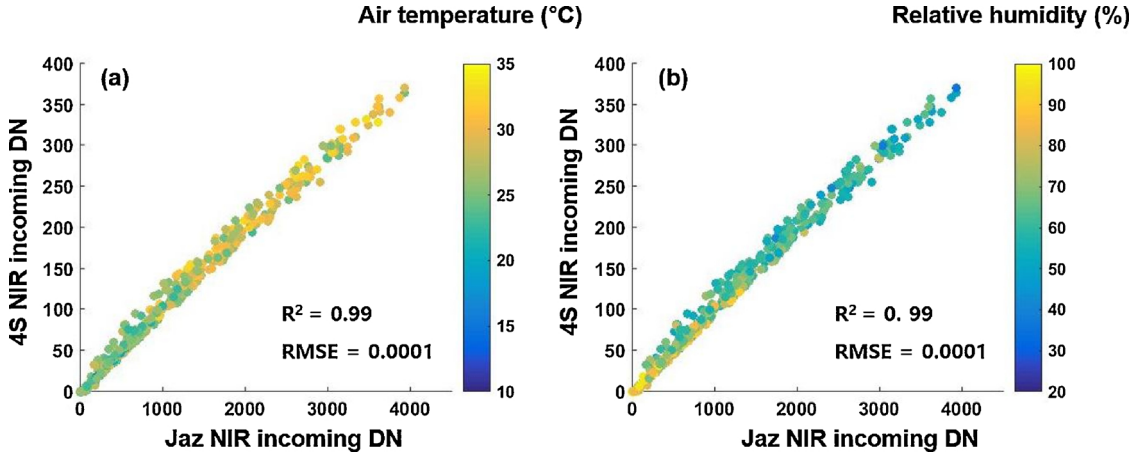

Fig. 6. Relationships between the Smart Surface Sensing System (4S) and Jaz spectrometer under a broad range of (a) temperature and (b) relative humidity, collected in the rice paddy site over the whole growing season.

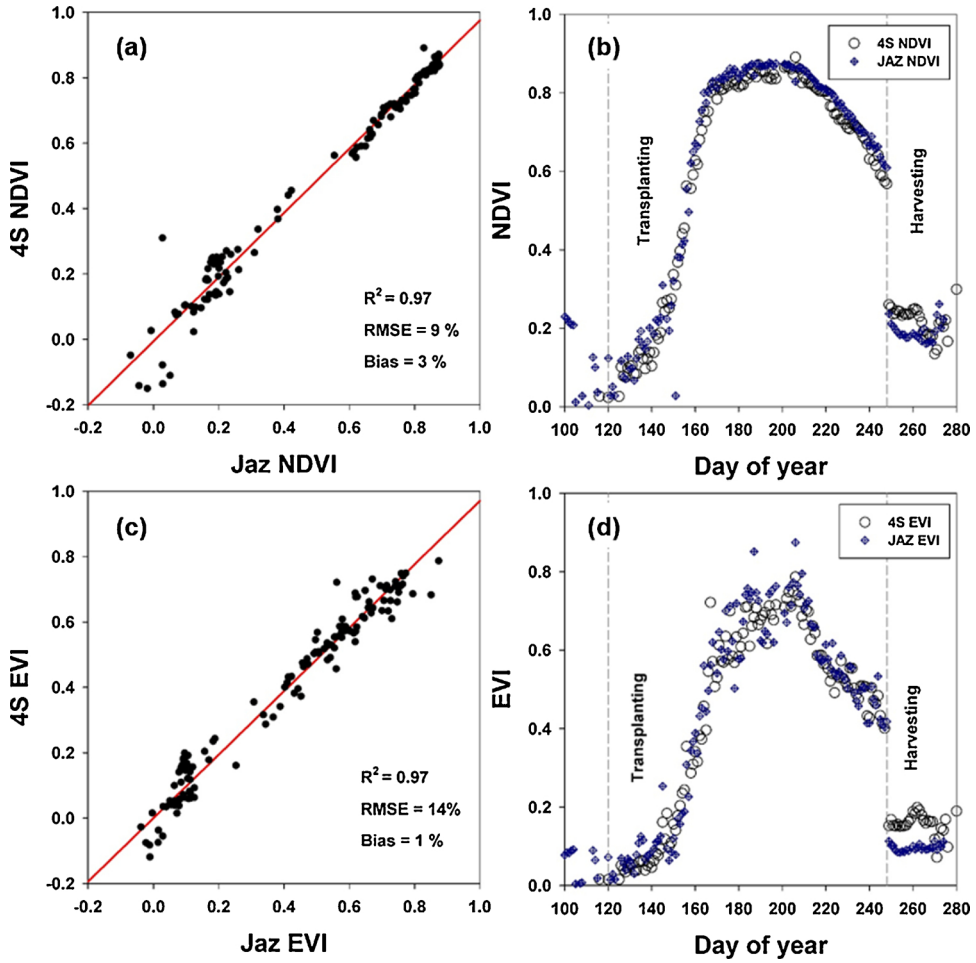

Fig. 7. Comparison of the Normalized Difference Vegetation Index (NDVI) and Enhanced Vegetation Index (EVI) observed at midday between the Smart Surface Sensing System (4S) and a Jaz spectrometer. We averaged the observed EVI and NDVI in four 4S. Graphs (a) and (c) illustrate scatter plots of results for the 4S and Jaz spectrometer. Graphs (b) and (d) represent seasonal variations in NDVI and EVI observed by the 4S and Jaz spectrometer.

(5%) and greatest with LAI-2200 LAI (–33%) (Fig. 10), indicating that 4S-based LAI_g tracked the seasonality of LAI_g using destructive method. Substantial uncertainty in destructive LAI (Fig. 9) could be explained by spatial heterogeneity of sampled LAI and imperfect leaf area estimates from scanned images.

Image-based GI allows estimation of LAI_g. Optical sensors, such as LED and LAI-2200, overestimated LAI_g during the ripening stage because the sensors measured not only green leaves but also yellow leaves, stems, and grains. To estimate LAI_g, we used GI, which can track changes in canopy colors (Keenan et al., 2014). We found that normalized GI mirrored the increase in the grain and yellow leaf area fractions during the senescence period (Fig. 10). We tested a range of

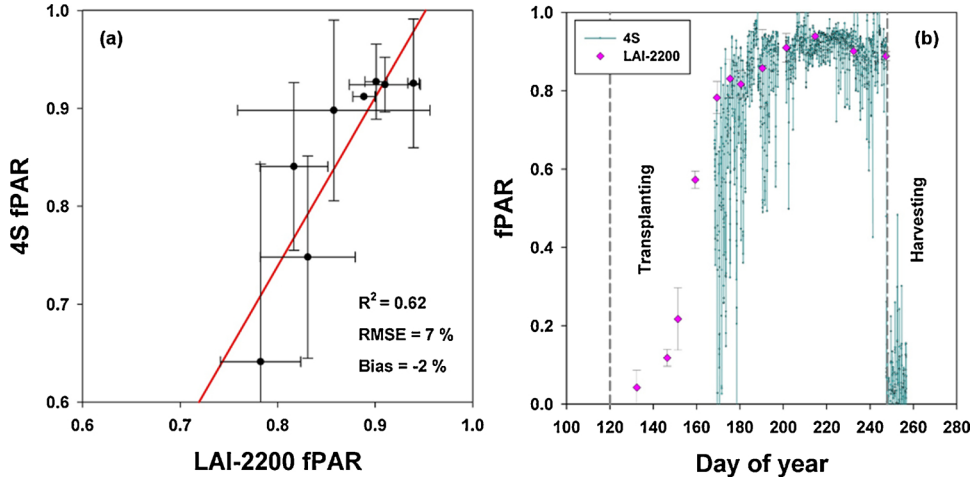

Fig. 8. (a) Scatterplot of the Fraction of absorbed Photosynthetically Active Radiation (fPAR) observed by the Smart Surface Sensing System (4S) and the LAI-2200. Red line indicates linear regression between the 4S and LAI-2200 data. Graph (b) represents time series of fPAR from the 4S and LAI-2200. Error bars indicate 95% CI.

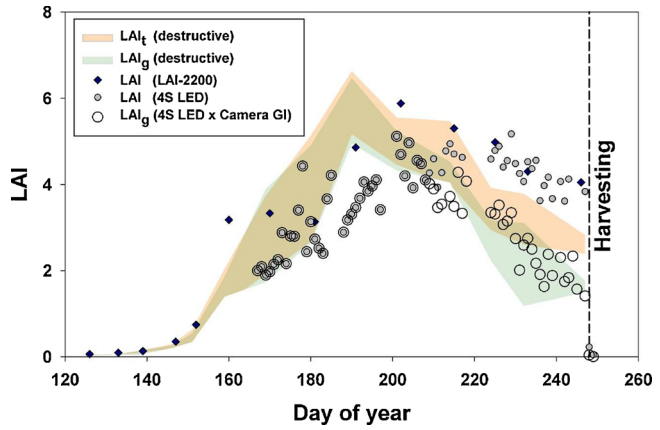

Fig. 9. Comparison of the Leaf Area Index (LAI) and green LAI (LAI g) estimated using the Smart Surface Sensing System (4S) with reference LAI, including destructive green LAI (LAIg), destructive total LAI (LAIt), and LAI-2200-derived LAI (LAI). The destructive LAI and LAI include 95% CI. To compute 4S LAIg, we multiplied 4S LAI by the normalized greenness index (GI) when GI began to decrease.

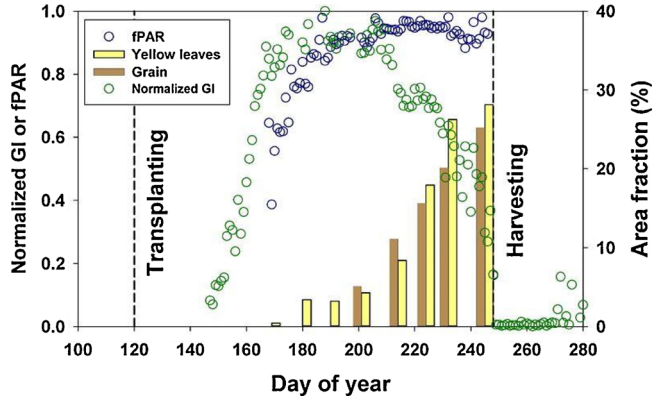

Fig. 10. The comparison of the Normalized Difference Vegetation Index (NDVI) and the fraction of absorbed Photosynthetically Active Radiation (fPAR) with the percentage of grain and yellow leaves. The dashed lines indicate transplanting and harvesting dates. As the grain began to form, fPAR remained constant, while NDVI decreased. To avoid overlapping bars, we used a 1-day time lag for displaying percentages of grains and yellow leaves.

different green indices from red, green and blue channels, and found the GI performed best in tracking green leaf fraction (Eq. (6)). We also tested if the Jaz spectrometer could track the green leaf fraction, but we learned that the spectrometer signal was influenced by background elements such as soil and other standing structure (Ide et al., 2016). However, 57° images taken from the 4S camera mostly captured the upper canopy with little influence of background elements. We believe continuously tracking LAI_g will result in more constrained estimates of GPP (Gitelson et al., 2014; Leuning et al., 1995). The fraction of LAI_g to LAI_t allows us to infer the green fPAR (Weiss et al., 2004). It was reported that green fPAR can be used to better estimate gross primary production in maize and soybean (Gitelson et al., 2014; Zhang et al., 2014) through quantification of light use efficiency of green leaves (Gitelson and Gamon, 2015).

Our assumption of the constant k and Ω_e over the growing season could lead to biased estimates of 4S LAI (Eq. (5)). It is apparent that 4S LAI tends to be lower than other LAI values up to DOY 200 (Fig. 9). A previous study reported that k varied among the phenological stages of rice, due to the changes in the leaf angle distribution (Casanova et al., 1998). In our rice paddy site, however, the mean leaf angle was manually measured using a levelled digital camera (Ryu et al., 2010c) that did not vary much over the season (50–70°, Appendix C). In a previous study, Ω_e also showed seasonal variation, gradually decreasing from the transplant period to the peak of the growing season and then rising again prior to the harvest (Fang et al., 2014). We found a small seasonal variation in Ω_e from the LED sensor and we could confirm that the apparent Ω_e from LAI-2200 with a 90° view cap and LED-based Ω_e falls within a similar range (0.88–0.95). Although the combined variations in k and Ω_e might influence 4S LAI estimates considerably, they were not detectable within the limits of our current system.

3.3. Implications for evaluating satellite remote sensing data

Continuous observation of NDVI with the 4S offered more insightful information when compared to remote sensing satellite-based NDVI. The 4S data set was less influenced by atmospheric conditions and clouds than satellites are, leading to fewer gaps in 4S data (Fig. 11). On average, 4S only missed 28 days of data during the 125-day growing season (Table 2). In contrast, the high-resolution remote sensing satellites Sentinel-2 and Landsat only captured six and two scenes, respectively, with good quality. Daily observation of MODIS Terra and Aqua contained 20% and 16% cloud-free data during the growing season. A previous study also reported that over 80% of MODIS data in regions with a monsoon climate, were affected by clouds. Therefore, combining multiple sources of satellite data is one possible solution to avoid cloud contamination (Motohka et al., 2009). It is now possible to use constellations of CubeSat to monitor land surface processes daily at 3- to 5-m resolutions (Houborg and McCabe, 2018). A ground-based spectral sensing network such as the 4S will be instrumental in testing and calibrating CubeSat surface reflectance data, which is prone to errors due to low radiometric qualities as well as a lack of consistency across the different sensor readings.

Continuous observation of NDVI at the plot scale demonstrated that high-spatial-resolution satellite remote sensing makes more accurate observations than does low-spatial-resolution satellite remote sensing. The 4S agreed best with Sentinel-2, the remote sensing dataset with the highest spatial resolution (R^2 = 0.99, relative bias = 3%), whereas MODIS Terra exhibited lower R^2 and higher bias (R^2 = 0.84, relative bias = 11%). We compared the MODIS NDVI value with the average value of Sentinel-2 NDVI pixels in the MODIS pixel that was included our study plot (Fig. 5a) (R^2 = 0.91, relative bias = 15%). The substantial bias (15%) measured indicates that we need to perform a calibration when combining Sentinel-2 and MODIS data (D'Odorico et al., 2013), which requires in-situ reference data. In addition, we found that the NDVI of the MODIS pixel tended to be overestimated after the harvest period, possibly due to the presence of four differently managed rice patches within the MODIS pixel. The 4S could serve as a high-resolution reference sensor in both space and time, playing an important role in the scaling of land surface fluxes at larger scales, by merging satellite images using multiple resolutions.

3.4. Opportunities

The 4S consists of relatively low-cost components that can be easily replicated and replaced (refer to Appendix A). Unexpected issues such as natural disasters in the field can lead to difficulty in collecting continuous data using near-surface remote sensors (Richardson et al., 2013). The best way to respond to such disturbances is to replace the sensor immediately. Low-cost sensors can reduce the burden related to securing sufficient spare sensors, which can be used to quickly replace sensors in the field. In

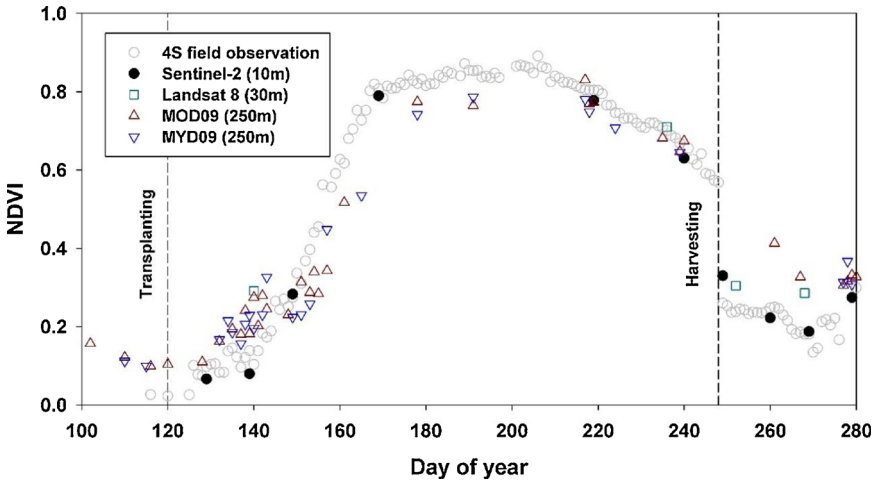

Fig. 11. Comparison of normalized difference vegetation index (NDVI) observed using the Smart Surface Sensing System (4S) and satellite data at different resolutions. From each satellite image, only a single pixel that includes the tower was selected.

addition, low-cost sensors provide the opportunity to install a larger number of sensors. Deployment of multiple sensors provides the potential to monitor variations in vegetation from plot to the regional scales (Qu et al., 2014b), and these sensors may also be installed in multiple layers to assess vertical canopy structure and functions (Ryu et al., 2014).

4S has the advantage of directly observing fPAR, VI, and LAI simultaneously. It has been common practice to infer one variable from the others. For example, a combination of PAR reflectance and shortwave reflectance was used as a proxy for NDVI (Rankine et al., 2017; Wilson and Meyers, 2007). LAI has been inferred from NDVI readings, based on their empirical relationships (Sellers, 1985; Yin et al., 2017) and fPAR was inferred from NDVI by assuming that their relationship is linear (Asrar et al., 1984; Sims et al., 2006) or from reflectance of specific wavelengths (Inoue et al., 2008). These empirical relationships are prone to errors. For example, we tested the relationships between fPAR and NDVI under different LAI and sky conditions (Fig. 12) and it was evident that their relationships varied with these conditions. In all four cases, NDVI was fairly constant around 0.8, while fPAR varied

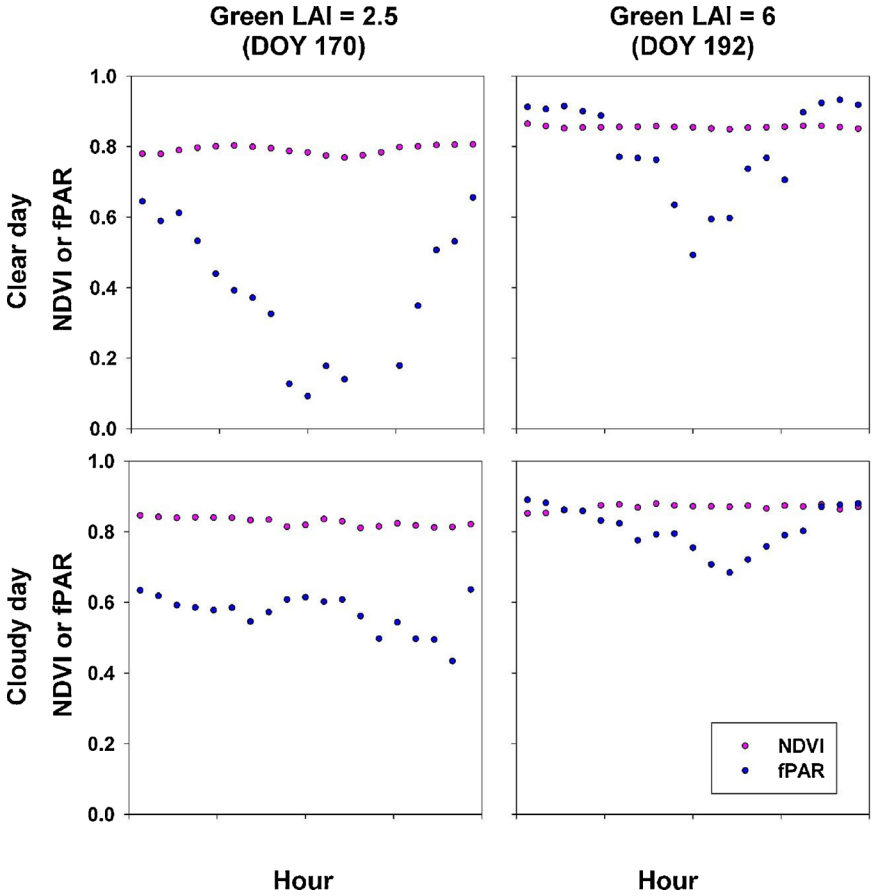

Fig. 12. Comparison of the diurnal patterns of the observed fraction of absorbed Photosynthetically Active Radiation (fPAR) with the Normalized Difference Vegetation Index (NDVI) on a clear and cloudy day. We averaged the observed fPAR and NDVI in three 4S sets (Fig. 5).

substantially in each case. These findings challenge the empirical model built upon a linear relationship between fPAR and NDVI.

The 4S camera can save images in a raw format, allowing better quantification of the canopy structure. The JPEG format, which is commonly used, has a non-linear relationship with light intensity because of gamma correction (Cescatti, 2007). However, the raw format shows a linear response to the intensity of light, so we can use it to quantify light intensity (Lang et al., 2010; Mullikin et al., 1994). In addition, the raw format stores the original image, providing greater bit depth resolution compared with JPEG format (Hwang et al., 2016; Macfarlane et al., 2014). We tested the response of the 4S DN camera against light intensity and confirmed their linear relationship (Appendix E). The dense canopy (LAI ~6) and oblique view angle (57°) in this study did not allow us to classify raw image pixels into vegetation and soil at the rice paddy site. We believe that the 4S camera has the potential to monitor gap fractions using raw images using a sky background, which has been tested across diverse sky and canopy structure conditions (Hwang et al., 2016).

4. Conclusion

There is a pressing need for the development of an inexpensive near-surface sensing network to concurrently monitor canopy structure and to function in multiple locations and across multiple biomes. Here, we developed a Smart Surface Sensing System (4S), which integrates an LED sensor, micro-camera, microcontroller and internet module to concurrently monitor VIs, fPAR, and LAI. Although the individual elements of the 4S are not new, integrating them into one system has allowed us to achieve an inexpensive yet reliable near-surface remote sensing system that monitors both canopy structure and functions simultaneously. Multi-channel LED sensors displayed a linear response to light intensity in the lab and were not sensitive to a range of temperature and humidity conditions in the field. We installed the 4S in a rice paddy site for the period of an entire growing season. We confirmed that the performance of the 4S was on par with that of Jaz spectrometers (VIs), LAI-2200 (fPAR and LAI) and destructive LAI (LAI_t and LAI_g) estimates. In particular, integrating gap fraction-based LAI estimates from LED sensors using a GI from the digital camera allowed for the tracking of seasonal variations in green LAI, which is an essential variable for monitoring crop growth. Furthermore, we found that 4S could be useful for evaluating satellite remote sensing products. We expect that the 4S will advance ecological sensing network research on multiple scales. All source codes and hardware information for 4S are open to public via https://github.com/Kinznice/Smart-Surface-Sensing-System.

Acknowledgements

This study was supported by the X Project, the National Research Foundation of Korea (NRF-2016R1E1A2A02946505) and the BK21 Plus Project in 2018 (Seoul National University Interdisciplinary Program in Landscape Architecture, Global leadership program towards innovative green infrastructure). Research Institute of Agriculture and Life Sciences at Seoul National University funded proofread service. We are grateful to our lab members who assisted with the calibration, installation and maintenance of the 4S at the rice paddy site. We thank Oliver Sonnentag for helping us to organize the paper better, Dennis Baldocchi and Joe Verfaillie for sharing his skills and knowledge in novel sensors/systems, Jane Lee for the final proofread, and NCAM staffs for jointly maintaining the field site.

Appendix A. List of components. Prices as of Aug. 2018

	Item	Q'ty	Unit price
Circuit	PCB board	2	$ 10.30
NIR band LED	OP296B	6	$ 1.70
Red band LED	SSL-LX5093SRD/D	6	$ 1.70
Green band LED	Any vendor	6	$ 1.70
Blue band LED	YK 3.0 mm Blue Lamps	6	$ 1.70
Amplifier	LTC1050CN8#PBF	12	$ 47.20
Amplifier holder	IM120807005	12	$ 15.80
Microcontroller	Arduino Nano	2	$ 9.80
Microcontroller socket	Single 1 × 15 Straight (2.54 mm)	3	$ 0.60
Cable	NT-IDC 6 pin cable (200 mm)	2	$ 1.90
Cable connector	Dual 2 × 3pin Straight (2.54 mm)	2	$ 0.60
Microcomputer	Raspberry pi 2	1	$ 38.60
Micro-camera	RGB V2 8 Megapixel	1	$ 26.40
Resistance 10 MΩ,1MΩ,0.67MΩ	–	12	$ 0.75
Micro SD card 16GB	SanDisk	1	$ 3.77
For Structure	Glass	1	$ 2.82
	Teflon	1	$ 1.41
	Aluminum boom	1	$ 23.54
	U bolt/nut	1	$ 14.12
	Case	1	$ 14.12
Sum			**$ 218.80**

Appendix B. Testing linear relationships of 4S against light intensity with time

See Fig. A1

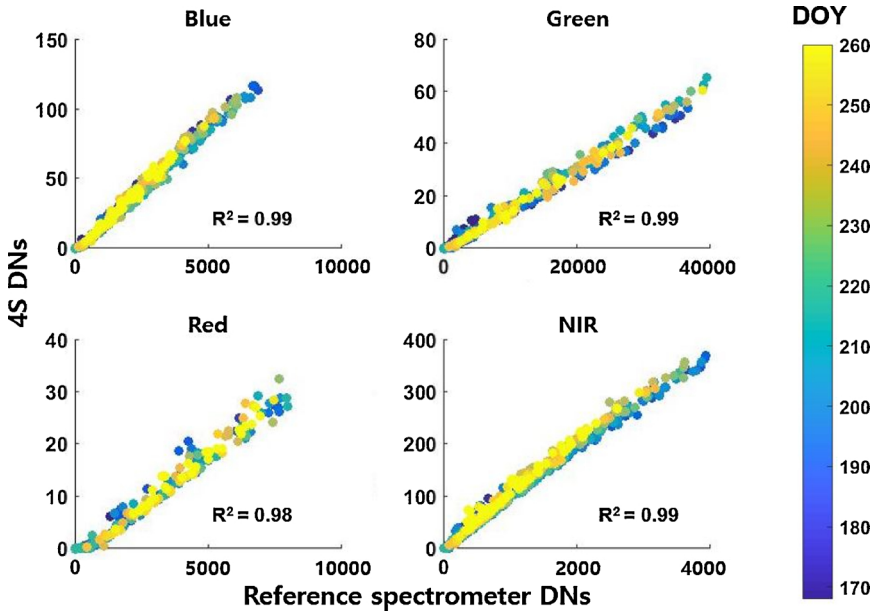

Fig. A1. Comparison of Digital Numbers (DN) between the reference spectrometer (Jaz) and 4S for both zenith directions. Half-hourly data during 0800 hh to 1600 hh between day of year (DOY) 166 and 262 were presented.

Appendix C. Extinction coefficient

We mainly followed the method of Ryu et al. (2014) to compute the extinction coefficient and clumping index in diffuse sky conditions. The extinction coefficient (k) depends on the leaf angle distribution function and the viewing zenith angle. We quantified leaf inclination angles using a leveled photographic method (Ryu et al., 2010c). During the 2017 growing season, we visited the rice paddy site every 10 days and randomly selected five hills. We removed each hill from the rice paddy and captured more than five pictures in the horizontal direction. In the lab, we only selected leaves indicated as lines in the images (Ryu et al., 2010c) and measured the angle between the leaf surface and its zenith for more than 250 leaves using ImageJ software (Ryu et al., 2014)(ImageJ; http://rsbweb.nih.gov/ij/). Mean leaf angles for each date in the growing season did not vary greatly (55 ± 1°, mean ± 95% CI). Therefore, we used all the values of leaf inclination angles observed during the growing season to calculate the probability density function of the leaf inclination angles, characterized using a two-parameter beta-distribution function (Goel and Strebel, 1984). We computed the G-function () to determine the extinction coefficient (Ryu et al., 2010c). Using Eq. A1 from Ryu et al. (2014) with input LAI of 2–7, we quantified $k(\theta)$ as 0.7 ± 0.017 (mean ± 95% CI).

Appendix D. 4S micro-camera images

See Fig. A2

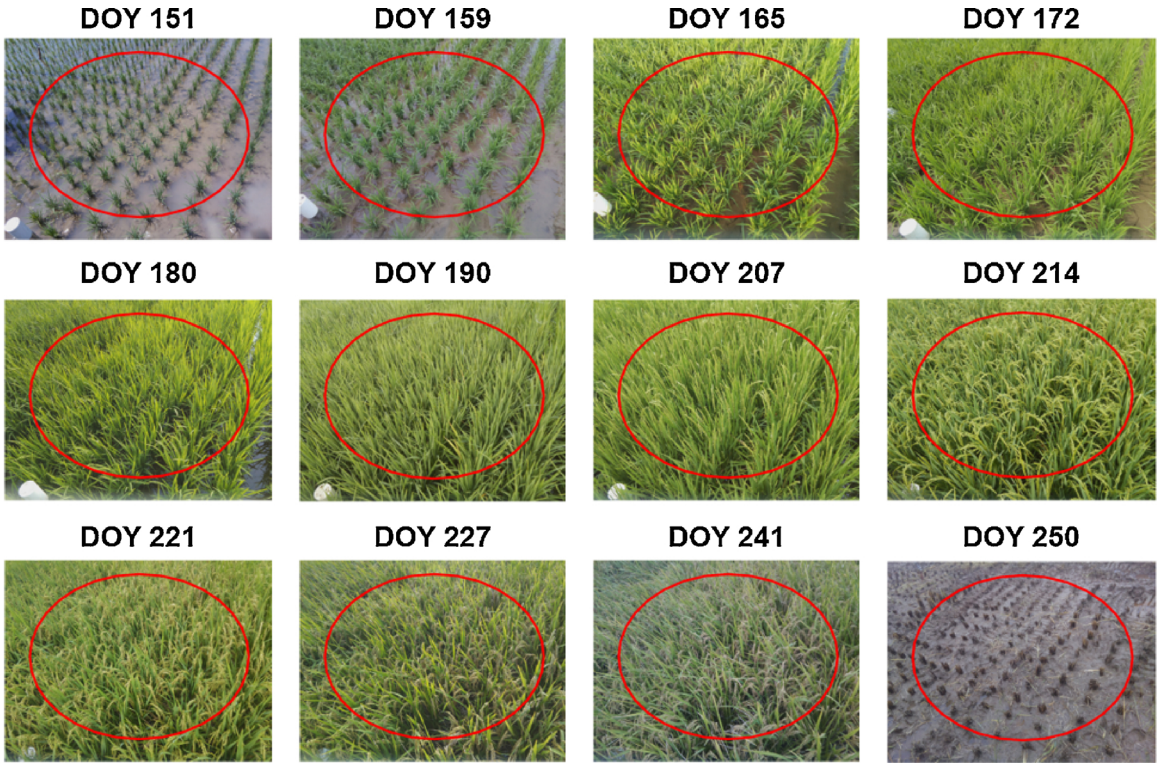

Fig. A2. Seasonal variations of phenology from the images of 4S micro-camera. The red circles indicate the Region Of Interest (ROI) for extracting Greenness Index (GI).

Appendix E. Testing the linear response of digital numbers in the 4S micro-camera

In order to evaluate the linear response of the micro-camera-to-light intensities, we compared raw DN divided by the shutter speed of the micro-camera to the spectral irradiance readings from a spectrometer (FieldSpec 4 Wide-Res Field Spectroradiometer, ASD, Inc., Boulder, CO, USA) across a wide range of radiation intensities. On a day with clear skies (DOY 223 in 2016), we installed a micro-camera covered by Teflon and the spectrometer, with its fiber optics covered by a cosine corrector, alongside each other on a rooftop in order to minimize the effect of shadows from surrounding structures. We then oriented both sensors to the zenith. We collected data at 10-minute intervals throughout the day under solar irradiances ranging from 60 to 1000 W m^{-2}. We extracted spectral irradiance values from the spectrometer at spectral ranges that corresponded to the peak values in each band of the camera (blue: 412 nm, green: 560 nm, red: 656 nm). The RAW DN divided by shutter speed of the micro-camera showed strong linear relationships with spectral irradiance from the spectrometer in the blue, green, and red bands (Fig. A3).

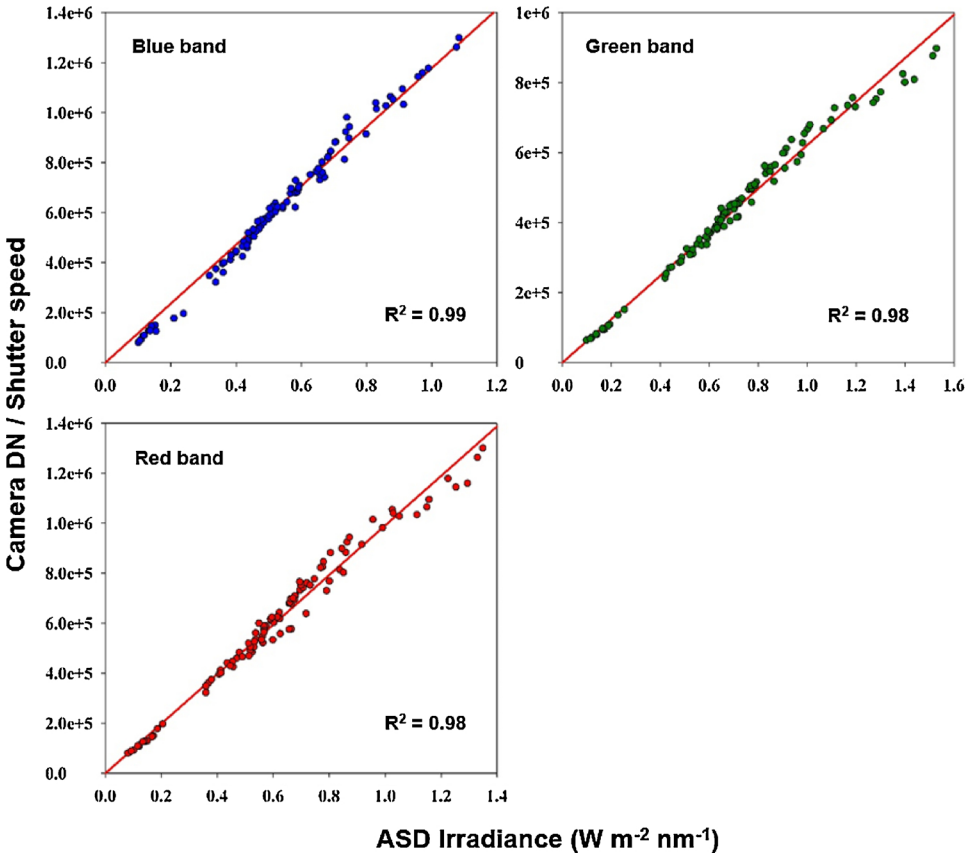

Fig. A3. Comparing the linear response of the ratio of Digital Numbers (DN) to the shutter speed in 4S micro-camera against a spectrometer (ASD Field Spec) across a wide range of conditions of solar radiation (60–1000 W m^{-2}) on a day with clear skies. The red line indicates the linear regression.

References

Asrar, G., Fuchs, M., Kanemasu, E., Hatfield, J., 1984. Estimating absorbed photosynthetic radiation and leaf area index from spectral reflectance in wheat. Agron. J. 76 (2), 300–306.

Baldocchi, D.D., Matt, D.R., Hutchison, B.A., McMillen, R.T., 1984. Solar radiation within an oak—hickory forest: an evaluation of the extinction coefficients for several radiation components during fully-leafed and leafless periods. Agric. For. Meteorol. 32 (3-4), 307–322.

Baldocchi, D.D., Wilson, K.B., Gu, L., 2002. How the environment, canopy structure and canopy physiological functioning influence carbon, water and energy fluxes of a temperate broad-leaved deciduous forest-an assessment with the biophysical model CANOAK. Tree Physiol. 22 (15), 1065–1077.

Baret, F., De Solan, B., Lopez-Lozano, R., Ma, K., Weiss, M., 2010. GAI estimates of row crops from downward looking digital photos taken perpendicular to rows at 57.5 zenith angle: theoretical considerations based on 3D architecture models and application to wheat crops. Agric. For. Meteorol. 150 (11), 1393–1401.

Bauer, J., Siegmann, B., Jarmer, T., Aschenbruck, N., 2014. On the potential of wireless sensor networks for the in-field assessment of bio-physical crop parameters. Local Computer Networks Workshops (LCN Workshops) 523–530.

Brusa, A., Bunker, D.E., 2014. Increasing the precision of canopy closure estimates from hemispherical photography: blue channel analysis and under-exposure. Agric. For. Meteorol. 195, 102–107.

Casanova, D., Epema, G., Goudriaan, J., 1998. Monitoring rice reflectance at field level for estimating biomass and LAI. Field Crops Res. 55 (1), 83–92.

Cescatti, A., 2007. Indirect estimates of canopy gap fraction based on the linear conversion of hemispherical photographs: methodology and comparison with standard thresholding techniques. Agric. For. Meteorol. 143 (1), 1–12.

Chen, J.M., Black, T., 1992. Defining leaf area index for non-flat leaves. Plant Cell Environ. 15 (4), 421–429.

Chen, J.M., Rich, P.M., Gower, S.T., Norman, J.M., Plummer, S., 1997. Leaf area index of boreal forests: theory, techniques, and measurements. J. Geophys. Res. Atmos. 102 (D24), 29429–29443.

D'Odorico, P., Gonsamo, A., Damm, A., Schaepman, M.E., 2013. Experimental evaluation of Sentinel-2 spectral response functions for NDVI time-series continuity. Ieee Trans. Geosci. Remote. Sens. 51 (3), 1336–1348.

Fang, H., Li, W., Wei, S., Jiang, C., 2014. Seasonal variation of leaf area index (LAI) over paddy rice fields in NE China: intercomparison of destructive sampling, LAI-2200, digital hemispherical photography (DHP), and AccuPAR methods. Agric. For. Meteorol. 198, 126–141.

Fang, H., Ye, Y., Liu, W., Wei, S., Ma, L., 2018. Continuous estimation of canopy leaf area index (LAI) and clumping index over broadleaf crop fields: an investigation of the PASTIS-57 instrument and smartphone applications. Agric. For. Meteorol. 253–254, 48–61. https://doi.org/10.1016/j.agrformet.2018.02.003.

Ferrández-Pastor, F., García-Chamizo, J., Nieto-Hidalgo, M., Mora-Pascual, J., Mora-Martínez, J., 2016. Developing ubiquitous sensor network platform using internet of things: application in precision agriculture. Sensors 16 (8), 1141. https://doi.org/10.3390/s16071141.

Gamon, J., Rahman, A., Dungan, J., Schildhauer, M., Huemmrich, K., 2006. Spectral network (SpecNet)—what is it and why do we need it? Remote Sens. Environ. 103 (3), 227–235.

Garrity, S.R., Vierling, L.A., Bickford, K., 2010. A simple filtered photodiode instrument for continuous measurement of narrowband NDVI and PRI over vegetated canopies. Agric. For. Meteorol. 150 (3), 489–496.

Gitelson, A.A., Gamon, J.A., 2015. The need for a common basis for defining light-use efficiency: implications for productivity estimation. Remote Sens. Environ. 156, 196–201.

Gitelson, A.A., Peng, Y., Arkebauer, T.J., Schepers, J., 2014. Relationships between gross primary production, green LAI, and canopy chlorophyll content in maize: implications for remote sensing of primary production. Remote Sens. Environ. 144, 65–72.

Goel, N.S., Strebel, D.E., 1984. Simple beta distribution representation of leaf orientation in vegetation canopies. Agron. J. 76 (5), 800–802.

Gressler, E., Jochner, S., Capdevielle-Vargas, R.M., Morellato, L.P.C., Menzel, A., 2015. Vertical variation in autumn leaf phenology of Fagus sylvatica L. In southern Germany. Agric. For. Meteorol. 201, 176–186. https://doi.org/10.1016/j.agrformet.2014.10.013.

Hilker, T., Coops, N.C., Nesic, Z., Wulder, M.A., Black, A.T., 2007. Instrumentation and approach for unattended year round tower based measurements of spectral reflectance. Comput. Electron. Agric. 56 (1), 72–84.

Houborg, R., McCabe, M.F., 2018. A Cubesat enabled Spatio-Temporal Enhancement Method (CESTEM) utilizing Planet, Landsat and MODIS data. Remote Sens. Environ. 209, 211–226.

Huang, Y., et al., 2018. BESS-Rice: a remote sensing derived and biophysical process-based rice productivity simulation model. Agric. For. Meteorol. 256–257, 253–269. https://doi.org/10.1016/j.agrformet.2018.03.014.

Huete, A., et al., 2002. Overview of the radiometric and biophysical performance of the MODIS vegetation indices. Remote Sens. Environ. 83 (1), 195–213.

Hwang, Y., et al., 2016. Correction for light scattering combined with sub-pixel classification improves estimation of gap fraction from digital cover photography. Agric. For. Meteorol. 222, 32–44.
Ide, R., Hirose, Y., Oguma, H., Saigusa, N., 2016. Development of a masking device to exclude contaminated reflection during tower-based measurements of spectral reflectance from a vegetation canopy. Agric. For. Meteorol. 223, 141–150.
Inoue, Y., Peñuelas, J., Miyata, A., Mano, M., 2008. Normalized difference spectral indices for estimating photosynthetic efficiency and capacity at a canopy scale derived from hyperspectral and CO 2 flux measurements in rice. Remote Sens. Environ. 112 (1), 156–172.
Jenkins, J., et al., 2007. Refining light-use efficiency calculations for a deciduous forest canopy using simultaneous tower-based carbon flux and radiometric measurements. Agric. For. Meteorol. 143 (1), 64–79.
Jiang, Z., Huete, A.R., Didan, K., Miura, T., 2008. Development of a two-band enhanced vegetation index without a blue band. Remote Sens. Environ. 112 (10), 3833–3845.
Jiang, C., et al., 2017. Inconsistencies of interannual variability and trends in long-term satellite leaf area index products. Glob. Chang. Biol. 23 (10), 4133–4146. https://doi.org/10.1111/gcb.13787.
Keenan, T., et al., 2014. Tracking forest phenology and seasonal physiology using digital repeat photography: a critical assessment. Ecol. Appl. 24 (6), 1478–1489.
Kobayashi, H., Ryu, Y., Baldocchi, D.D., Welles, J.M., Norman, J.M., 2013. On the correct estimation of gap fraction: how to remove scattered radiation in gap fraction measurements? Agric. For. Meteorol. 174–175, 170–183. https://doi.org/10.1016/j.agrformet.2013.02.013.
Lang, A., 1987. Simplified estimate of leaf area index from transmittance of the sun's beam. Agric. For. Meteorol. 41 (3-4), 179–186.
Lang, A., Yueqin, X., 1986. Estimation of leaf area index from transmission of direct sunlight in discontinuous canopies. Agric. For. Meteorol. 37 (3), 229–243.
Lang, M., Kuusk, A., Mõttus, M., Rautiainen, M., Nilson, T., 2010. Canopy gap fraction estimation from digital hemispherical images using sky radiance models and a linear conversion method. Agric. For. Meteorol. 150 (1), 20–29. https://doi.org/10.1016/j.agrformet.2009.08.001.
Leuning, R., Kelliher, F., Pury, Dd., SCHULZE, E.D., 1995. Leaf nitrogen, photosynthesis, conductance and transpiration: scaling from leaves to canopies. Plant Cell Environ. 18 (10), 1183–1200.
Liao, M.-S., et al., 2017. On precisely relating the growth of Phalaenopsis leaves to greenhouse environmental factors by using an IoT-based monitoring system. Comput. Electron. Agric. 136, 125–139.
Macfarlane, C., Ryu, Y., Ogden, G.N., Sonnentag, O., 2014. Digital canopy photography: exposed and in the raw. Agric. For. Meteorol. 197, 244–253.
Magney, T.S., Eitel, J.U., Huggins, D.R., Vierling, L.A., 2016. Proximal NDVI derived phenology improves in-season predictions of wheat quantity and quality. Agric. For. Meteorol. 217, 46–60.
Michalsky, J.J., 1988. The astronomical almanac's algorithm for approximate solar position (1950–2050). Sol. Energy 40 (3), 227–235.
Michalsky, J., Berndt, J., Schuster, G., 1986. A microprocessor-based rotating shadowband radiometer. Sol. Energy 36 (5), 465–470.
Monteith, J.L., 1965. Evaporation and environment. Symp. Soc. Exp. Biol. 4.
Motohka, T., Nasahara, K., Miyata, A., Mano, M., Tsuchida, S., 2009. Evaluation of optical satellite remote sensing for rice paddy phenology in monsoon Asia using a continuous in situ dataset. Int. J. Remote Sens. 30 (17), 4343–4357.
Mullikin, J.C., et al., 1994. Methods for CCD camera characterization. IS&T/SPIE 1994 International Symposium on Electronic Imaging: Science and Technology 12.
Mutanga, O., Skidmore, A.K., 2004. Narrow band vegetation indices overcome the saturation problem in biomass estimation. Int. J. Remote Sens. 25 (19), 3999–4014.
Myneni, R., Asrar, G., Kanemasu, E., 1987. Light scattering in plant canopies: the method of successive orders of scattering approximations (SOSA). Agric. For. Meteorol. 39 (1), 1–12.
Myneni, R.B., Ramakrishna, R., Nemani, R., Running, S.W., 1997. Estimation of global leaf area index and absorbed PAR using radiative transfer models. Ieee Trans. Geosci. Remote. Sens. 35 (6), 1380–1393.
Nagai, S., et al., 2014a. Relationship between spatio-temporal characteristics of leaf-fall phenology and seasonal variations in near surface- and satellite-observed vegetation indices in a cool-temperate deciduous broad-leaved forest in Japan. Int. J. Remote Sens. 35 (10), 3520–3536. https://doi.org/10.1080/01431161.2014.907937.
Nagai, S., et al., 2014b. Year-to-year blooming phenology observation using time-lapse digital camera images. J. Agric. Meteorol. 70 (3), 163–170.
Price, L.L.A., Hooke, R.J., Khazova, M., 2014. Effects of ambient temperature on the performance of CCD array spectroradiometers and practical implications for field measurements. J. Radiol. Prot. 34 (3), 655.
Qu, Y., et al., 2014a. LAINet – a wireless sensor network for coniferous forest leaf area index measurement: design, algorithm and validation. Comput. Electron. Agric. 108, 200–208. https://doi.org/10.1016/j.compag.2014.08.003.
Qu, Y., Zhu, Y., Han, W., Wang, J., Ma, M., 2014b. Crop leaf area index observations with a wireless sensor network and its potential for validating remote sensing products. Ieee J. Sel. Top. Appl. Earth Obs. Remote. Sens. 7 (2), 431–444.
Rankine, C., Sánchez-Azofeifa, G., Guzmán, J.A., Espirito-Santo, M., Sharp, I., 2017. Comparing MODIS and near-surface vegetation indexes for monitoring tropical dry forest phenology along a successional gradient using optical phenology towers. Environ. Res. Lett. 12 (10), 105007.
Raymaekers, D., et al., 2014. SPOT-VEGETATION GEOV1 biophysical parameters in semi-arid agro-ecosystems. Int. J. Remote Sens. 35 (7), 2534–2547. https://doi.org/10.1080/01431161.2014.883096.
Richardson, A.D., et al., 2007. Use of digital webcam images to track spring green-up in a deciduous broadleaf forest. Oecologia 152 (2), 323–334.
Richardson, A.D., Klosterman, S., Toomey, M., 2013. Near-surface sensor-derived phenology. Phenology: An Integrative Environmental Science. Springer, pp. 413–430.
Richardson, A.D., et al., 2018. Tracking vegetation phenology across diverse North American biomes using PhenoCam imagery. Sci. Data 5, 180028.
Ross, J., 1981. The Radiation Regime and Architecture of Plants Stands. Junk Pub.
Ryu, Y., et al., 2010a. Testing the performance of a novel spectral reflectance sensor, built with light emitting diodes (LEDs), to monitor ecosystem metabolism, structure and function. Agric. For. Meteorol. 150 (12), 1597–1606. https://doi.org/10.1016/j.agrformet.2010.08.009.
Ryu, Y., et al., 2010b. On the correct estimation of effective leaf area index: does it reveal information on clumping effects? Agric. For. Meteorol. 150 (3), 463–472.
Ryu, Y., et al., 2010c. How to quantify tree leaf area index in an open savanna ecosystem: a multi-instrument and multi-model approach. Agric. For. Meteorol. 150 (1), 63–76.
Ryu, Y., et al., 2011. Integration of MODIS land and atmosphere products with a coupled-process model to estimate gross primary productivity and evapotranspiration from 1 km to global scales. Global Biogeochem. Cycles 25 (GB4017). https://doi.org/10.1029/2011GB004053.
Ryu, Y., et al., 2012. Continuous observation of tree leaf area index at ecosystem scale using upward-pointing digital cameras. Remote Sens. Environ. 126, 116–125. https://doi.org/10.1016/j.rse.2012.08.027.
Ryu, Y., Lee, G., Jeon, S., Song, Y., Kimm, H., 2014. Monitoring multi-layer canopy spring phenology of temperate deciduous and evergreen forests using low-cost spectral sensors. Remote Sens. Environ. 149, 227–238. https://doi.org/10.1016/j.rse.2014.04.015.
Sellers, P.J., 1985. Canopy reflectance, photosynthesis and transpiration. Int. J. Remote Sens. 6 (8), 1335–1372.
Sellers, P., et al., 1997. Modeling the exchanges of energy, water, and carbon between continents and the atmosphere. Science 275 (5299), 502–509.
Sims, D.A., et al., 2006. Parallel adjustments in vegetation greenness and ecosystem CO2 exchange in response to drought in a Southern California chaparral ecosystem. Remote Sens. Environ. 103 (3), 289–303.
Sonnentag, O., et al., 2012. Digital repeat photography for phenological research in forest ecosystems. Agric. For. Meteorol. 152, 159–177.
Tucker, C.J., 1979. Red and photographic infrared linear combinations for monitoring vegetation. Remote Sens. Environ. 8 (2), 127–150.
Weiss, M., Baret, F., Smith, G., Jonckheere, I., Coppin, P., 2004. Review of methods for in situ leaf area index (LAI) determination: part II. Estimation of LAI, errors and sampling. Agric. For. Meteorol. 121 (1), 37–53.
Welles, J.M., Norman, J., 1991. Instrument for indirect measurement of canopy architecture. Agron. J. 83 (5), 818–825.
Wilson, T.B., Meyers, T.P., 2007. Determining vegetation indices from solar and photosynthetically active radiation fluxes. Agric. For. Meteorol. 144 (3), 160–179. https://doi.org/10.1016/j.agrformet.2007.04.001.
Yang, K., Ryu, Y., Dechant, B., Berry, J.A., Hwang, Y., Jiang, C., Kang, M., Kim, J., Kimm, H., Kornfeld, A., Yang, X., 2018. Sun-induced chlorophyll fluorescence is more strongly related to absorbed light than to photosynthesis at half-hourly resolution in a rice paddy. Remote Sens. Environ. 216, 658–673. https://doi.org/10.1016/j.rse.2018.07.008.
Yin, G., et al., 2017. Derivation of temporally continuous LAI reference maps through combining the LAINet observation system with CACAO. Agric. For. Meteorol. 233, 209–221.
Zhang, Q., et al., 2014. Estimation of crop gross primary production (GPP): fAPAR Chl versus MOD15A2 FPAR. Remote Sens. Environ. 153, 1–6.
Zhao, M., Running, S.W., 2010. Drought-induced reduction in global terrestrial net primary production from 2000 through 2009. Science 329 (5994), 940–943.
Zhen, J., Tripler, E., Peng, X., Lazarovitch, N., 2017. A wireless device for continuous frond elongation measurement. Comput. Electron. Agric. 140, 1–7. https://doi.org/10.1016/j.compag.2017.05.011.